

Kirigami Curvature DRAFT

S.R. Wilson
K.A. Seffen

December 3, 2017

Abstract

Kirigami differs from the well-known *origami* by allowing cuts and material removal from a physical sheet in addition to folding. This work explores the use of kirigami as a basis for transforming flat sheets into 3D shapes. By formulating the principles of kirigami with basic topology and differential geometry, a framework is developed for transforming a sheet between flat and curved configurations by through a “suturing” process. We demonstrate this process by designing and analyzing the pure kirigami unit cell. We find that this unit cell is a type of plane symmetric, 6R mechanical linkage. We analyze the kinematics of this linkage and illustrate one possible tessellation. We expect this system to find applications in morphing structures and robotics where transitions between curvature states are desired.

1 Gauss-Bonnet Theorem

Topological principles, however, are not concerned with physical materials: “rubber-sheet geometry” is just that—abstractions of objects in any dimension without resistance to large in-plane deformations. In order to move one rung down the ladder of abstraction, we seek a connection between the three-dimensional geometry of perforated sheets and their topology. This link is given by the Gauss-Bonnet Theorem, stated as

$$\int_S K dA + \int_{\delta S} k_g ds = 2\pi\chi. \quad (1)$$

K is the Gaussian curvature within the surface, S , and k_g is the geodesic curvature integrated over line elements, ds , along the boundary, δS , of S [?]. This curvature computation is equated to the topological invariant χ from ???. This form of the theorem applies to orientable, compact objects—conditions our kirigami structures must obey. This is an astounding result in differential geometry, a commandment for how objects must obey their topological invariant whilst undergoing deformation. A fundamental intuition of Gaussian curvature is essential for understanding the importance of morphing kirigami structures. Rather than merely changing the shape of an object, we can completely change its structural properties. For the perforated disc from ???, we can insert ?? into Eqn (1) to yield

$$\int_S K dA + \int_{\delta S} k_g ds = 2\pi(1 - g). \quad (2)$$

Thus, we have a relationship between the number of kirigami cuts in our general surface, and how the curvature along the boundaries and within the sheet must reflect the homotopic change when a hole is closed. For brevity, we can rewrite Eqn (2) as

$$\tau + \gamma = 2\pi(1 - g) \quad (3)$$

for use in subsequent discussion. For a closed surface without boundary, γ will remain exactly 0. For a kirigami cell each hole will add an additional boundary, and the material will always contain an external boundary with changing geodesic curvature to reflect the opening or closing of holes as shown in Fig. 1. Thus, changing g will manifest itself in a change in τ and γ .

2 Discrete Gauss Bonnet Theorem

In this study, we focus on objects that can be modeled as polyhedral sheets with rigid, planar facets. To better understand the shape of general kirigami structures,

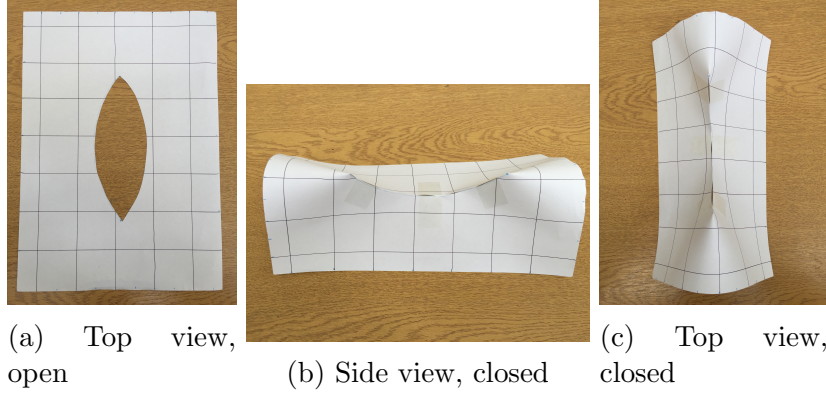


Figure 1: Thin sheet with a hole in open and closed configurations. This is the basic building block of a kirigami sheet transforming between two and three dimensions. In the closed configuration, the sheet’s external boundary must accommodate the change in genus g of the sheet.

we can develop a discrete form of Eqn (2) which is more efficient in computing the discrete curvature of polyhedral vertices. In its discrete form, we use angle measures and sums as opposed to integrals. We prove their equivalence and show in detail how they are used. For a discrete polyhedral surface, S , with boundary δS composed of n geodesics each of curvature k_g , it is straightforward to show

$$\sum_{i=1}^n \int_{\delta S_i} k_g \, ds = 0 \quad (4)$$

for each boundary edge δS_i . These edges are straight line segments (edges) with geodesic curvature 0. The boundary curvature is defined by the turning, or exterior, angles at the edge vertices, μ_{ext} , where

$$\mu_{ext}(v) = \pi - \sum_i \mu_i \quad (5)$$

for each $v \in \delta S$ where i facets converge. The Gauss-Bonnet Theorem for a polyhedral surface composed of planar facets can be rewritten as

$$\int_{\delta A} K \, dA + \sum_{v \in \delta S} \mu_{ext} = 2\pi(1 - g). \quad (6)$$

It can be shown that the Gaussian curvature concentrated at an interior polyhedral vertex v is exactly d , the angle defect of that vertex [?]. Since we restrict all facets

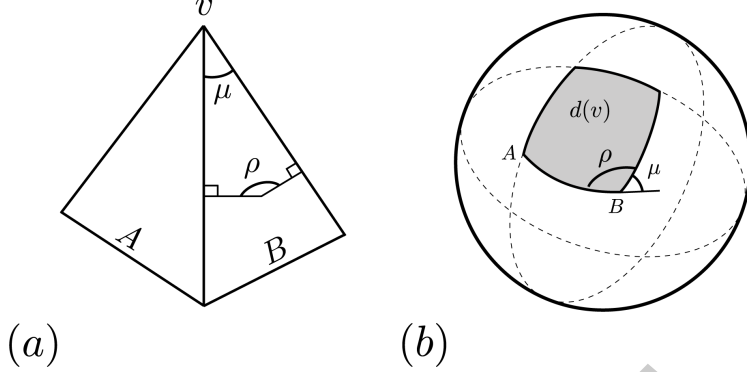


Figure 2: (a) Non-developable vertex, v , with angle defect, $d(v)$, positive curvature and facet angles μ . (b) The spherical map of the vertex. The defect of the vertex is shown as the area, $d(v)$, of the spherical quadrilateral with interior angles ρ . The facets A and B map to vertices on the spherical polygon.

to be rigid and planar for our kirigami, the integral of the Gaussian curvature over the surface is equal to the sum of the interior angle defects and each vertex defect is equal to the solid angle, A , subtended by a Gaussian spherical map of that vertex where

$$A = (2 - n)\pi + \sum_{i=1}^n \rho_i. \quad (7)$$

ρ_i is the interior angle of the i^{th} vertex of the spherical n -gon. It is trivial to show that μ_i , the interior angle of the i^{th} facet at polyhedral vertex v , is equivalent to $\pi - \rho_i$ making the angle defect, d , of that vertex

$$d(v) = 2\pi - \sum_{i=1}^n \mu_i. \quad (8)$$

The Gauss-Bonnet Theorem can thus be rewritten in discrete form as

$$\sum_{v \in S_{int}} d(v) + \sum_{v \in \delta S} \mu_{ext}(v) = 2\pi(1 - g) \quad (9)$$

for a polyhedral surface, S , with interior S_{int} and boundary δS . The parameters used in this derivation are shown in Fig. 2. A similar analysis has been employed in

computational geometry as a straightforward method of calculating discrete curvature for a polyhedral mesh [?]. We use this framework to explore the curvature of our kirigami unit cell. By constructing a series of Gauss maps, it becomes clear how the curvature of the surface changes throughout its transformation, and provides insight for how kirigami cells might be tessellated to form a globally curved shape. An important definition to state here is “developable”, in terms of a surface. A developable polyhedral surface contains no vertices with nonzero discrete Gaussian curvature. To flatten a non-developable surface, some tear or cut must be made within the surface. Note that a fold is developable, and thus a vertex through which a single fold passes has exactly zero curvature.

3 Polyhedral Unfolding

We define *pure kirigami* as the removal of material within the boundary of a finite sheet, and note that we subsequently use the term *kirigami* to mean this construction. What, then, are the limits of kirigami? While fold lines are prescribed within the sheet to allow for mobility, what collection of non-developable vertices can be created to produce a globally curved kirigami structure? This problem falls under a niche category of origami engineering known as polyhedral unfolding, a graph theory topic in disguise. We investigate several key results in that field to mathematically define kirigami and build a vocabulary to better understand the geometric constraints involved.

A graph is a collection of edges and vertices; a path is an ordered traversal of vertices on a graph through its edges; a cycle is a path that returns to its starting point. A tree is a graph with no cycles, and a forest is a disjoint collection of trees. Removing a single edge from a tree results in a forest. A cutting graph, or cutting, is a collection of edges on a simply connected polyhedral surface or closed polyhedron that separates faces of that surface or polyhedron. We seek cuttings that result in connected, flattened polyhedral surfaces called unfoldings. Specifically, we require unfoldings to not contain overlaps. Given a polyhedral surface, we can show that any unfolding is a forest, and that the cutting must traverse all vertices with nonzero curvature. By contradiction, if the cutting has a cycle, the unfolding will be disjointed. We want to retain the connectedness of our polyhedron in order to manufacture shapes from single sheets. Of course every polyhedral sheet has a trivial cycle along its boundary vertices, thus we exclude this case. If the cutting in question did not traverse all vertices with nonzero curvature, the faces joined by these vertices would not be flattenable. Thus, every nonzero curvature vertex must be included in the cutting.

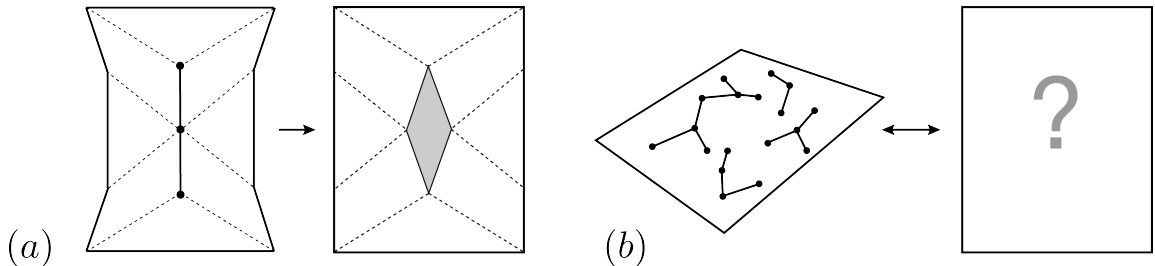


Figure 3: Statement of the general problem. (a) A single, fictitious kirigami cell in some folded and cut configuration. (b) Given a cutting forest, we seek a flattened kirigami geometry.

The flattened polyhedral surface need not be simply connected, thus the cutting need not be a tree. As shown in Fig. 3, a pure kirigami cell is a counterexample for this assumption. It is through connections of this type of component that we wish to create a global kirigami structure unfolded by a cutting forest. It has been proven that the requirement for this construction is nonconvexity [?]. We digress here to briefly define convexity with effort to do justice to the field of convex polytopes.

A set K of \mathbb{R}^n is convex if, for each pair of distinct points a, b in K , the closed segment with endpoints a and b is contained within K [?].

Another measure of convexity is the existence of “saddle corners”, or vertices of negative discrete Gaussian curvature [?].

Thus, for a closed, convex polyhedron, we know that, generally, the cutting must be a forest, and the connected graph condition of the cutting stems from the convexity condition. Assuming the cutting were a forest, one can imagine a closed contour on the polyhedron’s surface, across its faces, that encloses one of the forest’s trees entirely, avoiding any and all vertices of the polyhedron. When the cutting is made, this contour must unfold and flatten with the polyhedron meaning the sum of its turning angle, τ from Eqn (3), must equal 2π . From the closed condition, the left-hand side of Eqn (3) must be 2π . Due to the convexity condition, γ must be greater than or equal to zero (in the flattened state). However, since the contour must enclose at least one vertex of the polyhedron and the convexity condition enforces positive curvature on these vertices, γ must be strictly greater than zero. Since τ must be less than 2π to comply with Eqn (3), the polyhedron cannot flatten. Thus, the cutting of a convex polyhedron must be a tree. Note that every negative curvature vertex must be connected to two cut edges, as a single cut would allow

the faces of that vertex to overlap by its angle surplus. With these definitions and propositions defined, we apply this manner of thinking to explore what is possible for pure kirigami constructions.

4 Curvature of Kirigami Sheets

We would like to create kirigami structures with nonzero global curvature, an open polyhedron with some net angle defect, for double curvature is useful in creating shell structures with high strength to weight ratio such as spherical caps and saddles. This leads us to a question: does a polyhedral surface of some nonzero global curvature have a cutting that does not include any boundary vertices? In essence, we seek the existence of a non-developable structure with a cutting forest. We impose neither the convexity nor the closed condition on this structure, only that it has some nonzero net Gaussian curvature, no overlaps in the flattened state, and a disjoint cut tree. These are the requirements of a kirigami sheet in the language of graphs. We seek a flat sheet that can transform into a polyhedral shell or saddle by hole closures.

A kirigami object, by our definition, is a polyhedral sheet with a cutting forest that does not include any boundary vertices. For a kirigami object with net nonzero Gaussian curvature, every interior vertex would need to have nonzero curvature. Thus, every vertex would need to be traversed by a cutting forest. For the pure kirigami unit, we use the simplest hole, the rhombus cut, as shown in Fig. 3(a). This unit creates three vertices, one of negative curvature and two of positive curvature. As the hole is closed, the curvature of the internal boundary in the flat configuration must shift to the outer boundary in the closed configuration. In order to create a global sheet through the addition of these kirigami units, the boundary vertices of adjacent cells are connected. In order to retain the disjoint cutting, the boundary vertices must combine to form vertices with zero curvature. Since every interior vertex in a doubly-curved surface must have nonzero curvature vertices, this construction contradicts the constraints imposed by the disjoint cutting forest. In order to create doubly-curved kirigami, the boundary vertices of the sheet must be contained by the cutting or the sheet will not be developable. Stated formally, all bounded polyhedral surfaces with disjoint cut trees which disassemble their non-developable vertices have net-zero global curvature. Thus, pure kirigami can not be used to construct bounded polyhedral surfaces with double curvature. This does not mean that we cannot created singly curved or ruled surfaces using pure kirigami, which provides a rich design space. We explore this space in detail in ?? and ??.

5 Introduction

Kirigami, the art of cutting paper, has recently emerged as an alternative to origami for manufacturing three-dimensional (3D) geometries from two dimensions (2D). While origami has drawbacks such as excess material and intricate folds, kirigami techniques circumvent these difficulties by removing excess material and producing objects with simple folds. Information for 3D shapes is programmed into 2D sheets through the geometry of cuts. The principles underpinning these cuts are an active topic of research, and open questions remain, such as generalized cutting rules that will allow embedding of the sheet in three dimensions [?].

This work is motivated by the increasing demand for responsive architectures—interactive objects that respond to their environment. Research in this mode has presented shape-changing surfaces for aerodynamic designs, solar panels, and robotics [?, ?]. This work explores kirigami as a modular framework for transformable surface architecture. So-called “pluripotent” materials have been explored to produce out-of-plane geometry from kirigami, where the distribution of cuts made in a sheet are limited to a hexagonal graph and its triangular dual [?]. Rules are devised and experiments approximate curvature through the use of basic geometric building blocks. The result is a height map where the achievable gradient is limited by the size of the chosen unit cell. Similar schemes have been explored on the nano-scale using graphene [?].

Morphing structure design is rooted in repeating unit cell constructions. The geometry of the unit cell is analyzed and exploited through tessellation, such as the Miura-Ori geometry [?, ?, ?, ?]. The generalized problem of foldable sheets has been solved algorithmically, analytically, and computationally [?, ?, ?]. In robotics, the mathematical principles of folding have been applied to produce actuated structures [?, ?, ?]. In the generalized schemes, each polygonal element of the sheet is thought to be rigid or to allow bending of the first order [?].

This work rebuilds the foundations of kirigami from topological principles to its geometric implications, and results in the design and analysis of a kirigami unit cell. Links are drawn between kirigami and overconstrained linkages, and this similarity is employed to determine tessellation rules for multiple degree-of-freedom kirigami networks. We envision a reconfigurable surface composed of kirigami units that is able to change between a variety of global mode shapes. We hope for this work to elucidate the principles of morphing kirigami design and to find a variety of applications.

6 Unit Cell

Cutting a disc from a thin sheet and joining the edges of the hole together produces a minimal surface containing a saddle and two peaks [?]. Discretizing the disc into a rhombus results in the simplest hole that can be completely closed along straight edges. This is a form of the square lattice kirigami shown in Fig. 4. With the removal of two fold lines, we obtain a single degree of freedom mechanism containing a rhomboidal hole, as shown in Fig. 5. We first apply the discrete Gauss-Bonnet theorem to the vertices of the unit cell in the open configuration and the closed configuration. As the topology is fixed, we analyze the geometry of the cell using the vector parameterization shown in Fig. 5.

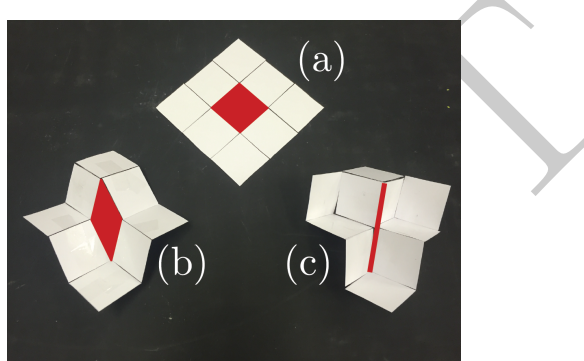


Figure 4: Basic square lattice kirigami. (a) Flat, unfolded annulus state. (b) Transition state. (c) Sutured disc state with hole fully closed.

In the open configuration, summing the interior angles and the exterior turning angles of Fig. 6 yields

$$[2(2\alpha) + 2(\pi - 2\alpha)] + [4(\pi - \alpha_{ext,2} + 2(\pi - \alpha_{ext,1})] = 2\pi\chi = 0 \quad (10)$$

where the exterior angles are:

$$\alpha_{ext,1} = \pi + 2\alpha, \quad \alpha_{ext,2} = \frac{3\pi}{2} - \alpha \quad (11)$$

and χ is 0 for an annulus; in the closed configuration χ is 1. The angular defect computation becomes a calculation of spherical polygon area, denoted A_{quad} and A_{tri} for the area of a spherical quadrilateral and triangle, respectively:

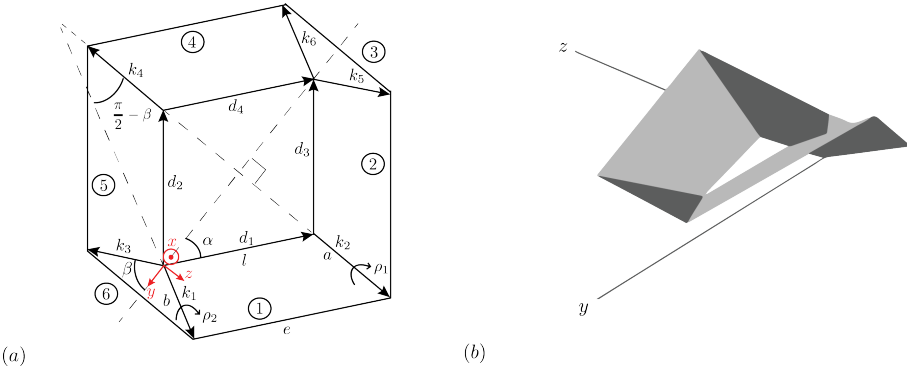


Figure 5: (a) Geometric parameterization of a one degree-of-freedom kirigami unit cell in its planar state. Vectors labeled k are fold lines; those labeled d are hole edges. (b) Rendering of the unit cell in a partially folded configuration. The origin (of the coordinates shown in red) is placed in the same position as in the parametric analysis.

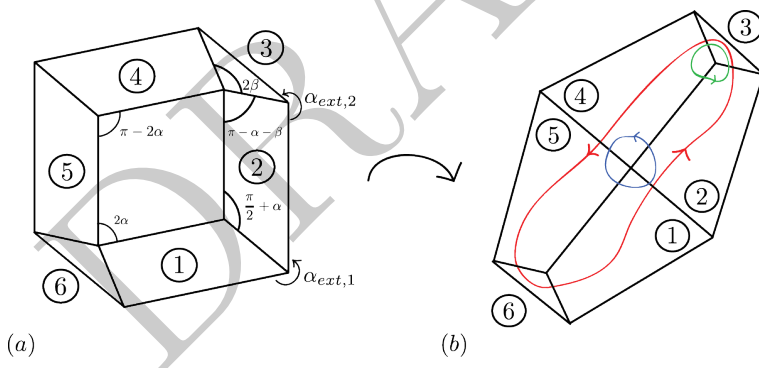


Figure 6: Two extreme states of the unit cell from Fig. 5. (a) The open planar state shows the unique interior and exterior vertex angles. (b) The closed configuration in plan view shows the contours used to produce Gauss maps. The green and blue contours yield the positive and negative Gauss maps for individual vertices, respectively, while the red contour yields the gauss map of the interior of the unit cell in its closed configuration. These maps are shown in Figs 7 and 8, respectively.

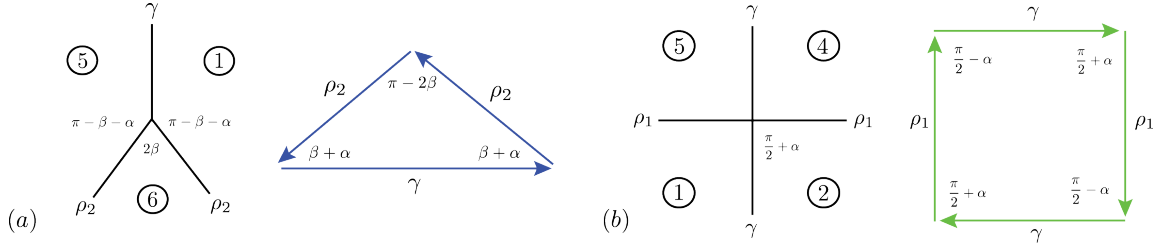


Figure 7: (a) One of two angular defect vertices in the interior of the closed until cell and its corresponding Gauss map. (b) The center saddle vertex of the closed unit cell and its corresponding Gauss map.

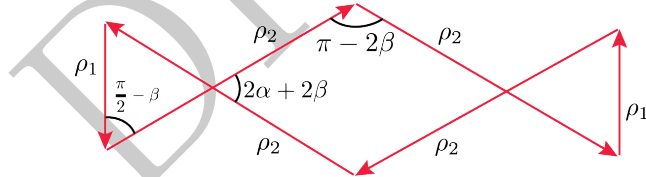


Figure 8: Gauss map of the three interior vertices in the closed configuration of the unit cell. The total solid angle as a sum of each signed area is zero; thus, the interior holds no net Gaussian curvature as expected.

$$A_{quad} = \sum_i^3 \alpha_i - 2\pi = 2(\pi - 2\beta) + 2(2\alpha + 2\beta) - 2\pi = 4\alpha \quad (12)$$

$$A_{tri} = \sum_i^3 \alpha_i - \pi = 2\left(\frac{\pi}{2} - \beta\right) + (2\alpha + 2\alpha) = 2\alpha. \quad (13)$$

Thus, the angular defect

$$d(v) = 2(2\alpha) - 4\alpha = 0 \quad (14)$$

where the center solid angle is negative due to its clockwise direction shown in Fig. 6. We see that the curvature, upon closing a cell, shifts to the exterior vertices and sums to 2π . By tessellating unit cells, we can take advantage of this curvature shift to construct a modular sheet with global shape by the combination of changing geometries.

7 6R Linkage

We identify an analogous linkage of the unit cell which is a special case of the 6R Bricard linkage [?], drawn in Fig. 9. A linkage with n bodies connected by g joints where joint i allows f_i freedoms is said to have a difference between mobility m and states of self-stress s according to the generalized Kutzbach criterion [?]

$$m - s = 6(n - 1) - 6g + \sum_{i=1}^g f_i. \quad (15)$$

The unit cell is deemed to have equal mobility and states of self-stress with six bodies connected by six single degree of freedom joints. By inspection, the linkage has zero states of self stress and must have zero mobility according to the generalized Kutzbach. However, the linkage has multiple mobility modes due to geometric symmetry. This overconstrained linkage is ideal for the purpose of a multiple degree of freedom sheet because it allows a single actuator to change the shape of a cell while influencing the global structure. To analyze the kinematics, we use a modified form of the Denavit-Hartenberg parameters [?]. Because all hinges lie in the plane for a kirigami sheet, we do not require homogenous coordinates to compute offset axes. All adjacent fold axes meet at a point, requiring just rotations around two axes, as shown in Fig. 9. Thus, each composite transformation is a 3x3 orthogonal matrix

$$T_{ij} = \begin{bmatrix} \cos \theta_i & -\sin \theta_i & 0 \\ \cos \alpha_i \sin \theta_i & \cos \theta_i \cos \alpha_i & -\sin \alpha_i \\ \sin \alpha_i \sin \theta_i & \cos \theta_i \sin \alpha_i & \cos \alpha_i \end{bmatrix} \quad (16)$$

where T_{ij} is the transformation from link i to link j shown in Fig. 9. Using symmetry, we set two opposing composite transformations equal to find a closure condition for the linkage

$$[T_{12}][T_{23}][T_{34}] = [T_{61}]^T[T_{56}]^T[T_{45}]^T \quad (17)$$

where the sector angles α and fold angles θ about the x and z axes shown in Fig. 9 adhere to the following relationships

$$\begin{aligned} \alpha_1 = \alpha_2 = \alpha_4 = \alpha_5 = \frac{\pi}{2} - \beta; \quad \alpha_3 = \alpha_4 = 2\beta \\ \theta_1 = \theta_3 = \theta_4 = \theta_6 = \rho_2; \quad \theta_2 = \theta_5 = \rho_1. \end{aligned} \quad (18)$$

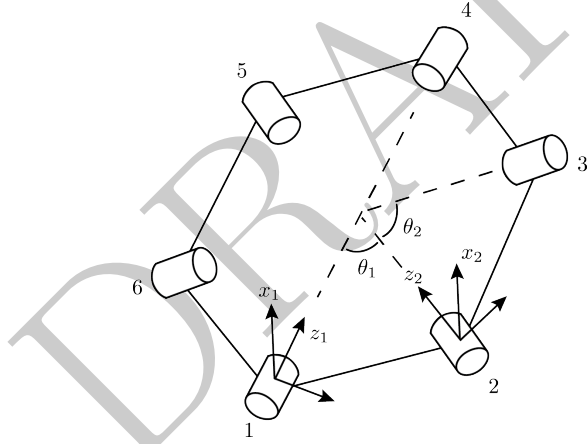


Figure 9: The 6R linkage analog to the kirigami unit cell, shown in its initial planar configuration. Coordinate transformations are made from joint 1 to joint 4 in both directions around the loop to generate a closure condition based on a modified Denavit-Hartenburg protocol.

By analyzing the closure condition in Eqn (17), we identify a periodic isosurface which visualizes the continuous motions of the linkage as a function of β , the geometric hinge angle, governed by

$$\begin{aligned}
& \sin \rho_1 \sin \rho_2 + \sin^3 \beta + \cos 2\beta \sin \beta \cos \rho_2 + \sin^3 \beta \cos \rho_1 \cos^2 \rho_2 \\
& + \cos 2\beta \sin \beta \cos \rho_1 \cos \rho_2 - \cos^2 \beta \sin \beta \cos \rho_1 - \sin \beta \cos \rho_1 \sin \rho_2^2 \\
& - 2 \cos^2 \beta \sin \rho_1 \sin \rho_2 - \cos^2 \beta \sin \beta \cos^2 \rho_2 - 2 \sin^2 \beta \cos \rho_2 \sin \rho_1 \sin \rho_2 = 0.
\end{aligned} \tag{19}$$

The isosurface informs the configuration of each individual unit cell by providing an input-output relationship. Given a geometric angle β and one hinge angle, we can solve for the third unknown hinge angle which completely describes the state of the cell at any given geometry and configuration. This will inform a network of cells by providing the ability to describe the configuration of any cell within a tessellation. We plot this isosurface and numerically find the value for β for the minimum area closure loop, shown in Fig. 10. If we assume the flexural hinges in the kirigami cell to act as linear-elastic beams for a first approximation, strain energy scales linearly with hinge width. Thus, the minimum area kinematic loop is thought to correspond to the least energy geometry, the geometric design with the least amount of motion to achieve continuous transformation of the linkage.

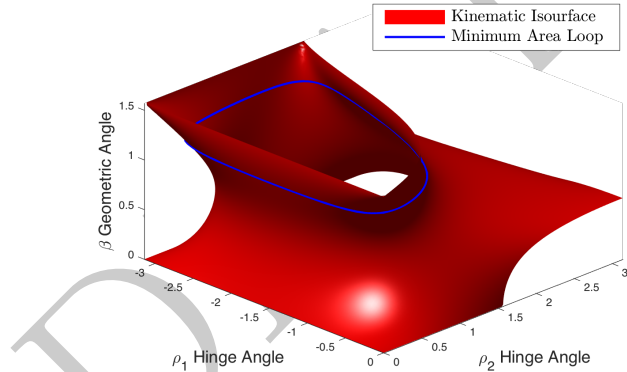


Figure 10: The isosurface is shown in red, which provides all continuous solutions given a geometric quantity β for the linkage as a function of ρ_1 and ρ_2 shown in Fig. 5. The minimum area solution for β is found and plotted as a contour in blue.

8 Tessellation

We describe a preliminary tessellation structure of the unit cell in one and two dimensions. The one dimensional network of cells is shown in various configurations

in Fig. 11. By actuating n cells independently, we have 2^n possible configurations in one dimension. For a surface that is able to morph into a plethora of shapes, we seek a method of linking 1D strands together. In Fig. 12, we offer one method of tessellating in two dimensions that involves snubbing the hexagonal units into octagons and rotating the fold lines of the original unit by $\frac{\pi}{2}$. This tessellation shows promise in creating a sheet with n degrees of freedom from n unit cells. However, this pattern creates a pattern of rectangular cuts that affect the shear strength of the sheet. This may be mitigated by altering the geometry of the unit cells, and is being explored.

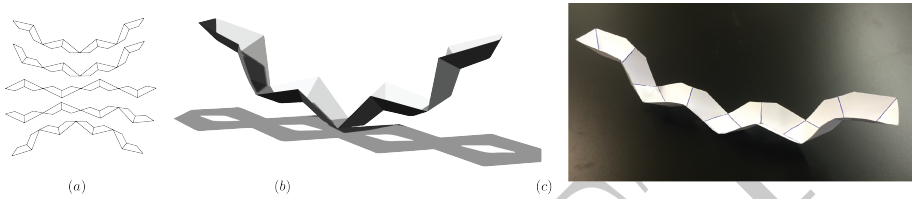


Figure 11: (a) For a one dimensional tessellation with n units, we have 2^n configurations, with five shown. By adjusting the geometry of the unit, we can create tessellations in a range of shapes. (b) Rendering of one configuration. (c) Physical prototype.

The current geometric and linkage analysis informs only the unit cell kinematics and geometry. In order to design a network of kirigami linkages, we must take a combinatorial approach to the problem to efficiently generate a list of geometrically plausible networks. It is nontrivial to extend a 1D tessellation into 2D due to self intersection and non-developability constraints. We can then experiment with tessellations to understand their transformations by combining the constituent unit cell kinematics. In order to devise a set of feasible tessellations, we are currently exploring methods of abstracting unit cell connections in order to systematically formulate the problem. This combinatorial formulation remains our principle challenge.

9 Conclusion

We present preliminary work towards a new approach for kirigami engineering utilizing unit cell construction. Using basic differential geometry, we illustrate how a shift in curvature for a polyhedral unit cell occurs when changing homotopy groups. We outline a framework for creating surfaces exploiting this curvature shift that are

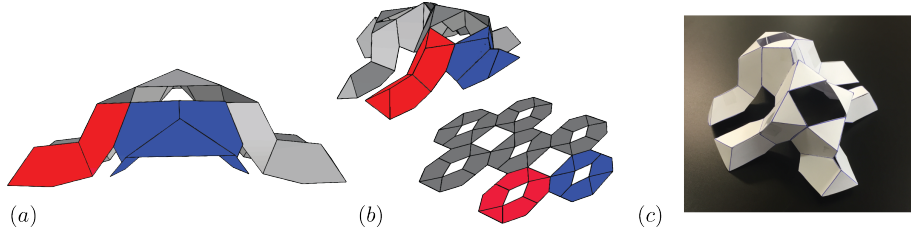


Figure 12: A possible tessellation in two dimensions. All units are closed in the same sense here, approximating a doubly curved sheet. The tessellation uses two unique unit cells shown in red and blue, with hinge lines rotated by $\frac{\pi}{2}$. (a) Side view of the tessellation. (b) Isometric view with the unfolded configuration. (c) Physical model.

able to morph in a general manner using modular units. By creating a network of n continuously kinematic linkages, we propose an n -degree of freedom surface for unit-by-unit, distributed actuation to produce an array of shapes. By characterizing the motion of the unit cell, we can combine cells to describe the shape of the actuated network.

This method of shape change is likened to muscle architecture, and could show promise in the generation of undulatory motion. Using a regular pattern of kirigami cuts with irregular closure patterns over the sheet, this scheme is the foundation for a distributed actuation of a patterned sheet in order to produce a variety of shapes. The authors are working to build a working prototype to physically realize the design and identify new problems.

References

References

We experimented with unit cells analogous to 8R linkages in ???. For a sheet with embedded actuators, it is difficult to control two degrees of freedom per unit cell when one of the degrees of freedom is nonplanar. By removing two fold lines, we change the unit cell topology, decrease the degrees of freedom, and create an overconstrained 6R kirigami linkage containing a rhombus hole. We name this cell the “octopus” cell due to its form and motion as shown in Fig. 13.

10 Mobility and Symmetry

We begin an analysis of the octopus cell by investigating its mobility. We identify a special case of the general 6R Bricard linkage analogous to the unit cell drawn in ???. The unit cell is deemed to have equal mobility and states of self-stress with six bodies connected by six single degree of freedom joints. By inspection, the linkage has zero states of self stress and must have zero mobility according to the generalized Kutzbach criterion. However, the linkage has multiple mobility modes due to geometric symmetry. This overconstrained linkage is ideal for the purpose of a morphing sheet because it allows a single actuator to change the shape of a cell while influencing the global shape of the structure. This cell has two symmetry planes; we can create a contact polyhedron C shown in Fig. 14(a) to apply the symmetry-extended mobility formulae described in ???. By inspection the cell has three folding modes: two symmetric and one antisymmetric shown in Fig. 15. We seek these of these modes through representation calculations. For the doubly symmetric cell, the lowest point group symmetry is C_s , with one symmetry plane. The character table for this group is supplied in Table 1. Using the C_s character table, we calculate the representations in Table 2. The identity operation, E , does not displace any nodes, thus the difference between the mechanism and self stress representations is zero, while the symmetry plane provides a difference of two. Since the cell is known to have the same number of mechanisms and self-stresses, due to symmetry there exist two mechanisms and two corresponding self-stresses. From the character table, these mechanisms must belong to a symmetric mode, A' , and an antisymmetric mode, A'' , where

$$\Gamma(m) - \Gamma(s) = A'' - A'. \quad (20)$$

Since the representations must be positive, the mechanism here is due to a symmetry and an antisymmetry, $A'' + A'$ and the self stresses are $A' + A'$. This means the

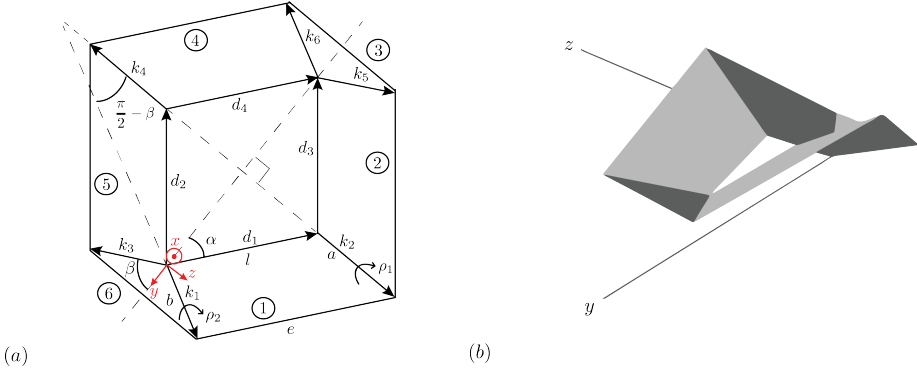


Figure 13: (a) Geometric parameterization of a one degree-of-freedom kirigami unit cell in its planar state. Vectors labeled k are fold lines; those labeled d are hole edges. (b) Rendering of the unit cell in a partially folded configuration. The origin (of the coordinates shown in red) is placed in the same position as in the parametric analysis.

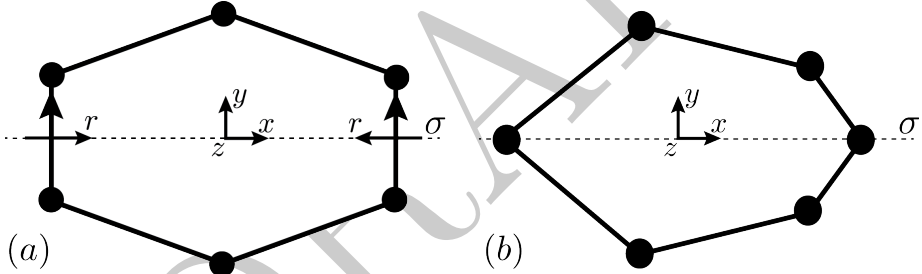


Figure 14: The contact polyhedra, C , for symmetry calculations. (a) C for the doubly symmetric linkage. (b) C for the singly symmetric linkage.

Table 1: The C_s character table.

C_s	E	σ
A'	1	1
A''	1	-1

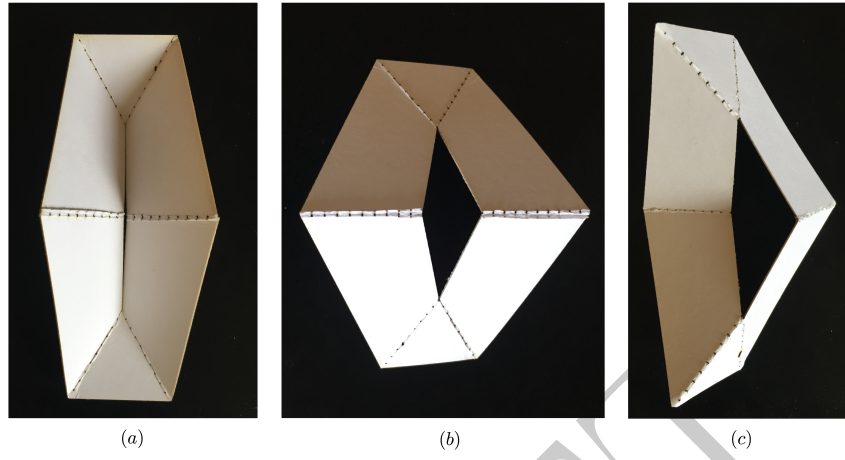


Figure 15: Paper prototype showing three mobility modes of the octopus cell. (a) Primary symmetric mode. (b) Secondary symmetric mode. (c) Antisymmetric mode.

Table 2: The symmetry calculation for the symmetric octopus cell.

$\Gamma(m) - \Gamma(s) =$	E	σ
$\Gamma(v, C)$	6	0
$\times \Gamma_T + \Gamma_R$	$\times 6$	$\times 0$
$- \Gamma_{\parallel}(e, C)$	-6	$-(-2)$
$\times \Gamma_T + \Gamma_R$	$\times 6$	$\times 0$
$-\Gamma_T + \Gamma_R$	-6	0
$+ \Gamma_f$	6	2
=	0	2

representation calculation shows one symmetric mechanisms and one antisymmetric, with two symmetric self stresses. We can imagine these self stresses being due to hinge misalignment in a translational or rotational sense. This calculation is repeated to explore the mechanisms of the singly-symmetric cell, which is of interest for the design of curved sheets. The contact polyhedron is shown in Fig. 14(b). The singly-symmetric cell's plane of symmetry, σ , does not pass through any hinge lines. The representation calculation is shown in Table 3 and results in no mechanisms since all hinge lines are permuted by the reflection operation. The resulting representation

Table 3: The symmetry calculation for the asymmetric octopus cell.

$\Gamma(m) - \Gamma(s) =$	E	σ
$\Gamma(v, C)$	6	2
$\times \Gamma_T + \Gamma_R$	$\times 6$	$\times 0$
$- \Gamma_{\parallel}(e, C)$	-6	0
$\times \Gamma_T + \Gamma_R$	$\times 6$	$\times 0$
$- \{\Gamma_T + \Gamma_R\}$	-6	0
$+ \Gamma_f$	6	0
=	0	0

equation reveals

$$\Gamma(m) - \Gamma(s) = 0 \times A' + 0 \times A''. \quad (21)$$

Thus, there are no symmetric or antisymmetric modes. This is surprising given the ability of the singly symmetric cell to close as shown in Fig. 25. Note that the symmetry-extended mobility rule is a necessary but not sufficient condition for mobility, thus there can still exist finite mechanisms in spite of the formula's outcome [?]. In this case, a close inspection of the cell reveals slight compliance in the facets. The magnitude of the necessary compliance to mobilize the singly-symmetric kirigami loop is discussed in subsection 11.1. Given the lowest symmetry group, C_s , for the cell, there is a descent in symmetry between differing planes, σ , which allows for the mobility of the linkage. This fact is useful in the parametric design of repeating lattice structures, as altering the symmetry of neighboring cells has a profound impact on the mobility of the global network. A simple conclusion we can draw from this

analysis is to design symmetry through hinge lines to allow mobility. This simple rule could play a powerful role in the design of future kirigami tessellations.

11 Geometry

To explore the consequences of the fold line removal, we investigate the discrete curvature of the unit cell vertices by applying the discrete Gauss-Bonnet theorem in the open and closed configurations. In the open configuration, summing the interior

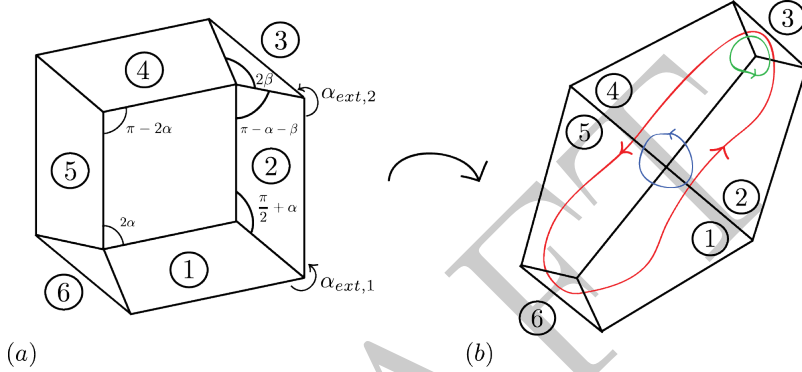


Figure 16: Open and closed states of the unit cell from Fig. 13. (a) The open, planar configuration shows the unique interior and exterior vertex angles. (b) The closed configuration shows the contours used to produce Gauss maps. The green and blue contours yield the positive and negative Gauss maps for individual vertices, respectively, while the red contour yields the gauss map of the interior of the unit cell in its closed configuration. These maps are shown in Figs 17 and 18, respectively.

rhombus angles and the exterior turning angles of Fig. 16 yields

$$[2(2\alpha) + 2(\pi - 2\alpha)] + [4(\pi - \alpha_{ext,2} + 2(\pi - \alpha_{ext,1}))] = 2\pi\chi = 0 \quad (22)$$

where the exterior angles are:

$$\alpha_{ext,1} = \pi + 2\alpha, \quad \alpha_{ext,2} = \frac{3\pi}{2} - \alpha. \quad (23)$$

In the open configuration, the cell is an annulus and χ is 0. In the cell's closed configuration, χ becomes 1. The angular defect computation becomes a calculation

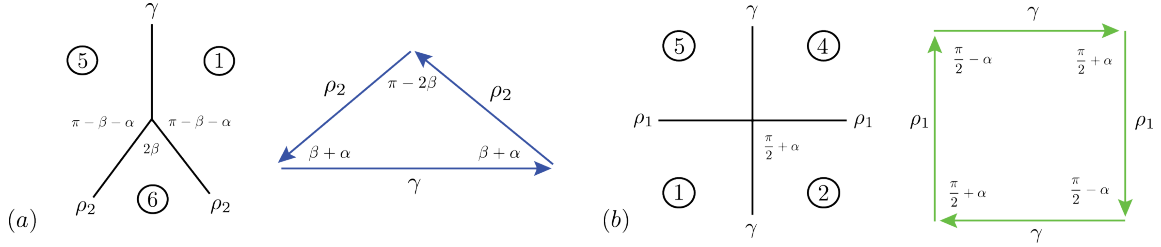


Figure 17: (a) One of two angular defect vertices in the interior of the closed until cell and its corresponding Gauss map. (b) The center saddle vertex of the closed unit cell and its corresponding Gauss map.

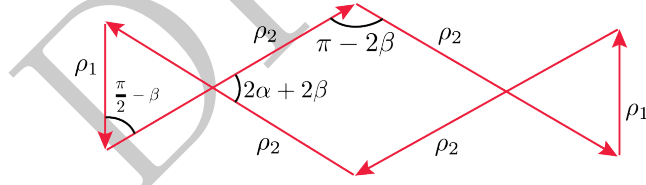


Figure 18: Gauss map of the three interior vertices in the closed configuration of the unit cell. The total solid angle as a sum of each signed area is zero; thus, the interior holds no net Gaussian curvature as expected.

of spherical polygon area, denoted A_{quad} and A_{tri} for the area of a unit spherical quadrilateral and triangle, respectively:

$$A_{quad} = \sum_i^3 \alpha_i - 2\pi = 2(\pi - 2\beta) + 2(2\alpha + 2\beta) - 2\pi = 4\alpha \quad (24)$$

$$A_{tri} = \sum_i^3 \alpha_i - \pi = 2\left(\frac{\pi}{2} - \beta\right) + (2\alpha + 2\alpha) = 2\alpha. \quad (25)$$

Thus, the angular defect is

$$d(v) = 2(2\alpha) - 4\alpha = 0 \quad (26)$$

where the center solid angle is negative due to its clockwise direction shown in Fig. 16. The curvature, upon closing a cell, shifts to the exterior vertices and sums to 2π . This is a continuous phenomenon; the spherical map changes throughout the cell's closing. By tessellating unit cells, we can take advantage of this curvature shift to construct a modular sheet with global shape through the combination of changing geometries. By imagining the spherical polygons created throughout the cell's motion, this discrete curvature approach gives us an intuitive sense of the kinematics in terms of angle defects and spherical maps to design networks of unit cells. We now turn to a vector parameterization of the cell in order to calculate the shape of a cell with a given geometry.

11.1 Vector Parameterization

As the topology is fixed, we analyze the geometry of the cell using the vector parameterization shown in Fig. 13. Using vector analysis, we can produce geometric relationships between the cell's components for use in structural design. By placing vectors along hinge lines and the hole edges, we can keep track of the facet positions throughout the cell's motion. The Rodrigues rotation formula is a straightforward method of rotating a general vector \mathbf{v} about an axis \mathbf{k} by angle θ according to the right-hand rule [?]

$$\mathbf{v}_{\text{rot}} = \mathbf{v} \cos \theta + (\mathbf{k} \times \mathbf{v}) \sin \theta + \mathbf{k}(\mathbf{k} \cdot \mathbf{v})(1 - \cos \theta). \quad (27)$$

When the unit cell is in the closed configuration, we find a relationship between the dihedral angles, ρ_i and sector angles, 2β and $\frac{\pi}{2} - \beta$, for one half of a cell where ρ_2 is a function of α and β

$$\cos(\rho_{2,\text{closed}}) = \frac{\sin(\alpha + 2\beta) - \sin \alpha}{2 \sin \alpha \cos^2 \beta + 2 \cos \alpha \cos \beta \sin \beta}. \quad (28)$$

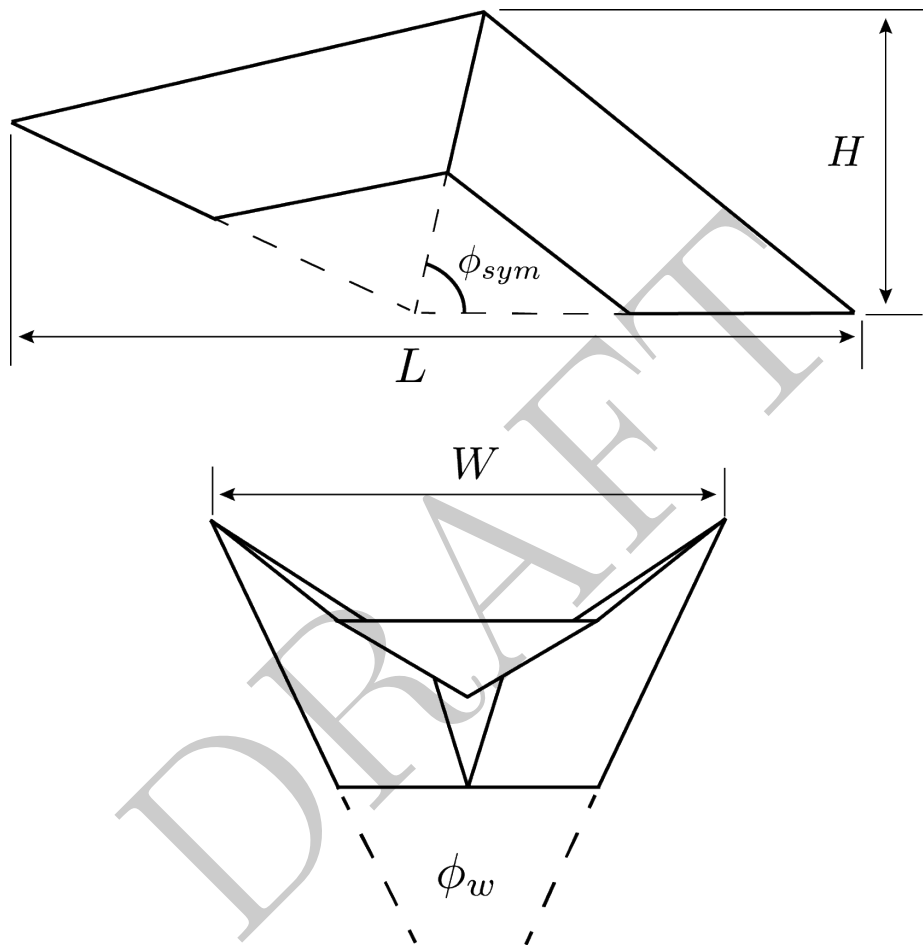


Figure 19: Side and front view of the unit cell with parametric values shown.

For the closed cell, we find the angle, ϕ_w between the normalized vectors \hat{k}_1 and \hat{k}_2 that span the middle plane

$$\begin{aligned}\hat{k}_1 \cdot \hat{k}_2 &= \cos \phi_w \\ &= 4 \cos^2 \beta - 2 \cos^4 \beta - 4 \cos^2 \beta \cos \rho_{2,\text{closed}} \\ &\quad + 4 \cos^4 \beta \cos \rho_{2,\text{closed}} - 2 \cos^4 \beta \cos^2 \rho_{2,\text{closed}} - 1\end{aligned}\tag{29}$$

where $\rho_{2,\text{closed}}$ is the dihedral angle in the closed configuration. Substituting Eqn (28) into Eqn (29), we find ϕ_w as a function on α and β only

$$\cos \phi_w = -\frac{\cos 2\beta - \cos 2\alpha + \sin 2\alpha \sin 2\beta}{\cos(2\alpha + 2\beta) - 1}.\tag{30}$$

For each half of the unit cell to match, the angle, ϕ_w spanned in the middle plane must match. For the singly-symmetric cell, this condition is violated. From Eqn (30), we see that changing α while holding β constant will lead to a twisting of the cell's facets on the order of the change in α due to the change in ϕ_w . Changing the length of one side of the unit cell changes $\cos \alpha$, stretching one side of the cell and removing the second plane of symmetry, leading to twisting of the facets. By keeping the antisymmetric change small, we can limit the facet twisting to a trivial level. While the symmetry formula yields zero mobility for the singly-symmetric unit cell, through experimentation we find very small compliance in the cell when it is moved into the closed position shown in Fig. 25. With apt material selection and geometric design, it may prove useful for morphing structures despite its necessary deformation. By attaching a local coordinate system shown in Fig. 13, we find relationships for H and W shown in Fig. 19 throughout the cell's motion where

$$\begin{aligned}H &= \|\sin \rho_2(l \sin(\alpha + \beta) + b \cos \beta)\| \\ W &= 2l \|\sin \alpha - \cos^2 \beta \sin \alpha + \cos^2 \beta \sin \alpha \cos \rho_2 \\ &\quad - \cos \alpha \cos \beta \sin \beta + \cos \alpha \cos \beta \sin \beta \cos \rho_2\| \\ &\quad + 2b \|\cos^2 \beta \cos \rho_2 - \cos^2 \beta + 1\|\end{aligned}\tag{31}$$

for the height and width, respectively, of the cell throughout its deployment. The middle plane spanned by the hinges k_1 and k_4 is described by the normal \hat{n} , shown in Fig. 19. We find \hat{n} using the cross product of k_1 and k_2 such that

$$\hat{n} = \begin{bmatrix} \frac{\sin \beta \sqrt{1-\cos \rho_2}}{\sqrt{(\cos^2 \beta \cos \rho_2 - \cos^2 \beta + 2)}} \\ -\frac{\sin \rho_2}{\sqrt{(1-\cos \rho_2)(\cos^2 \beta \cos \rho_2 - \cos^2 \beta + 2)}} \\ 0 \end{bmatrix}.\tag{32}$$

We find a relationship for the middle plane angle, ϕ_s , shown in Fig. 19 as a function of \hat{n}

$$\phi_s = \frac{\pi}{2} - \arccos(\hat{n} \cdot -\hat{y}). \quad (33)$$

where \hat{y} is the unit vector in the y coordinate direction. Computing this relationship for ϕ_s yields

$$\cos(\phi_s) = \frac{\sqrt{\frac{4 \cos(2\alpha+2\beta)-4 \cos 2\beta}{\cos 2\alpha-2 \cos 2\beta+2 \cos(2\alpha+2\beta)+\cos(2\alpha+4\beta)-2}}}{\sqrt{\frac{3 \sin(\alpha+\beta)-\sin(\alpha-\beta)}{\sin(\alpha+\beta)}} \sqrt{\frac{\sin \alpha}{\sin \alpha+\sin(\alpha+2\beta)}}}. \quad (34)$$

Using this relationship, we can find an expression for the length of the cell

$$L = 2R_z^{\phi_s}((|d_1| + |k_1| + |k_2|) * \hat{y}) \quad (35)$$

where $R_z^{\phi_s}$ is a rotation around the z axis by ϕ_s and $*$ is element-wise multiplication. We leave this expression in its symbolic form as the equations become quite long. The process to calculate these geometric relationships numerically is straightforward.

12 Linkage Analysis

To analyze the kinematics, we use a modified form of the Denavit-Hartenberg parameters [?]. For the kirigami cell where the structure begins in a flat configuration where all adjacent fold axes meet at a point, the protocol outlined in ?? requires only rotations around two axes, as shown in ??, where the sector angles α and fold angles θ about the x and z axes shown in ?? adhere to the following relationships

Table 4: Denavit-Hartenberg parameters for the general 6R kirigami linkage.

Link	α	a	θ	d
1	$\frac{\pi}{2} - \beta$	0	ρ_2	d
2	$\frac{\pi}{2} - \beta$	0	ρ_1	0
3	2β	0	ρ_2	d
4	$\frac{\pi}{2} - \beta$	0	ρ_2	d
5	$\frac{\pi}{2} - \beta$	0	ρ_1	0
6	2β	0	ρ_2	d

To simplify the analysis we set d to 0 for all links, effectively shrinking the rhombus hole to a point, converting the kirigami cell into a degree-6 origami vertex. This

way we simplify our calculations to focus on the angle relationships, summarized as

$$\begin{aligned} \alpha_1 = \alpha_2 = \alpha_4 = \alpha_5 = \frac{\pi}{2} - \beta, \alpha_3 = \alpha_6 = 2\beta \\ a_i = 0 \\ \theta_1 = \theta_3 = \theta_4 = \theta_6 = \rho_2, \theta_2 = \theta_5 = \rho_1 \\ d_i = 0 \end{aligned} \quad (36)$$

Compared to the Bricard linkages listed in ??, the kirigami linkage is a type of plane-symmetric linkage as confirmed from the mobility approach in Section 10. Using these parameters, we compute transformation matrices between each of the six coordinate systems. Our loop closure condition based on the C_s symmetry of the cell,

$$R_{12}R_{23}R_{34} = R_{16}R_{65}R_{54} \quad (37)$$

yields six equations where R_{ij} is the transformation matrix from coordinate system i to j . As there is one independent geometric parameter for the sector angles, β , and two parameters, ρ_1 and ρ_2 , for the hinge angles, there is only one independent loop closure equation:

$$\begin{aligned} & \sin \rho_1 \sin \rho_2 + \sin^3 \beta + \cos 2\beta \sin \beta \cos \rho_2 \\ & + \sin^3 \beta \cos \rho_1 \cos^2 \rho_2 + \cos 2\beta \sin \beta \cos \rho_1 \cos \rho_2 \\ & = \\ & \cos^2 \beta \sin \beta \cos \rho_1 - \sin \beta \cos \rho_1 \sin^2 \rho_2 \\ & - 2 \cos^2 \beta \sin \rho_1 \sin \rho_2 - \cos^2 \beta \sin \beta \cos^2 \rho_2 - 2 \sin^2 \beta \cos \rho_2 \sin \rho_1 \sin \rho_2. \end{aligned} \quad (38)$$

This relationship between the three independent angular parameters of the kirigami unit cell serves as an input-output relationship. By defining the geometry of the cell through β , we can solve for the unknown hinge angle given a certain configuration. This relationship can be plotted as an isosurface of possible configurations for the linkage as shown in Fig. 20. The function is 2π periodic as we would expect, though for physical solutions we assume that ρ_1 is between $-\frac{\pi}{2}$ and 0, ρ_2 is between 0 and $\frac{\pi}{2}$, and β is between 0 and $\frac{\pi}{4}$. The isosurface visualizes the solution space of these parameters. As we can see, there are solutions for all β beginning from $(\rho_1, \rho_2) = (0, 0)$ as well as a separate solution set beginning from $\beta = \frac{\pi}{4}$. By choosing two variables, we can numerically solve for the third, which allows us to completely characterize our unit cell in any geometry and configuration. For a given β , there exists a contour of solutions as a function of the kinematic variables, the kinematic path.

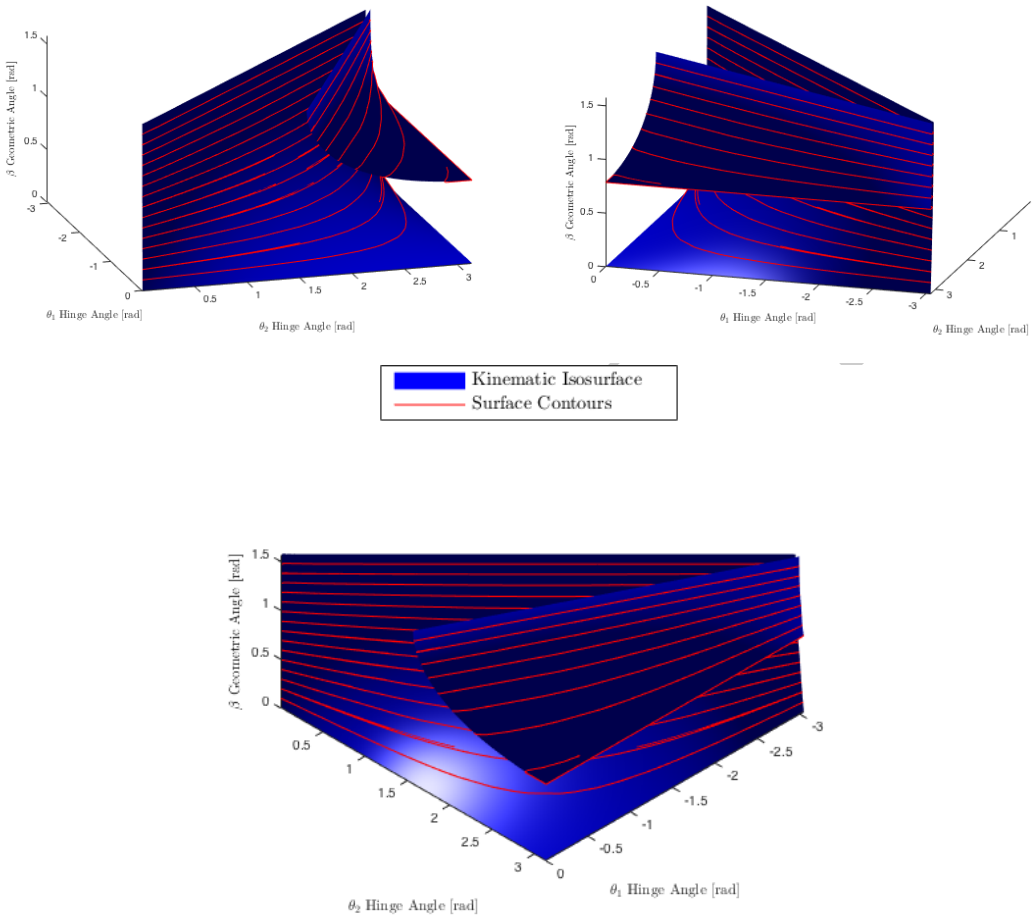


Figure 20: Three views of the three-dimensional isosurface shown in blue, which provides all continuous solutions given a geometric quantity β for the linkage as a function of ρ_1 and ρ_2 . Contours on the surface are shown in red.

13 Octopus Networks

Given a single degree of freedom unit cell, we explore tessellations of this cell, or linkage networks. Beginning in one dimension, we can tile the cells end-to-end to achieve an n degree of freedom structure with n connected cells. This structure can take 2^n configurations seeing as shown in Fig. 21. By snubbing the corners of the octopus cell, we can tile the octagons by rotating the fold lines of the original cell. This tessellation is one degree of freedom regardless of the number of cells in the network. The hinge lines provide constraints along each edge which sets the configuration of the neighboring cell. We note that given the additional, non-actuated “holes” in this octagonal tessellation, double curvature may be achieved using non-regular cells, as shown in Fig. 22. However, this is not “pure” kirigami as we have previously defined given the additional voids in the sheet. Utilizing the angle defined by the geometric parameters of the cell, we develop a ring structure of one degree of freedom which lifts out of plane upon closing the voids in the cells. The radius and height of this structure can be controlled simply by the geometry of the individual cells and the number included in the tessellation as shown in Fig. 23.

To test the feasibility of physical cells, we fabricate a unit cell from 3mm high-

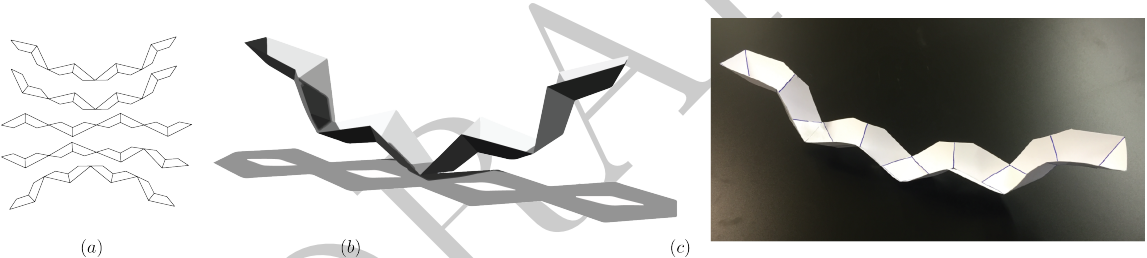


Figure 21: (a) For a one dimensional tessellation with n units, we have 2^n configurations, with five shown. By adjusting the geometry of the unit, we can create tessellations in a range of shapes. (b) Rendering of one configuration. (c) Physical prototype.

density polyethylene (HDPE) using a Roland MDX-40 micro-milling machine. The cell functions as expected with hinges of 1mm thickness. The physical cell is shown in the flat and deployed states in Fig. 24. For tessellations, a larger CNC machine could be used to produce a meter-scale tessellation in a short time. We wish to tessellate the 6R kirigami cell without the addition of extra holes as in the case of the 2D octagonal tessellation. To achieve this, we design a hexagonal cell able to tile without voids in singly symmetric and doubly symmetric versions as shown in Fig. 26 with

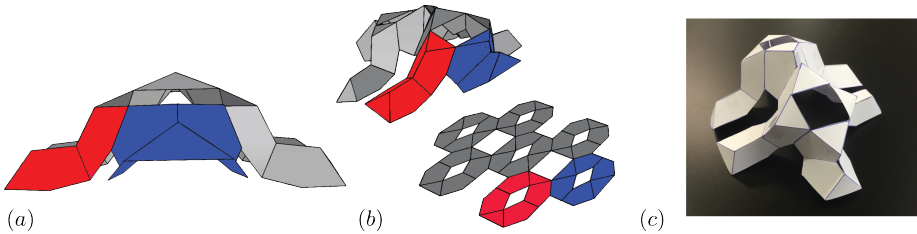


Figure 22: A possible tessellation in two dimensions. All units are closed in the same sense here, approximating a doubly curved sheet. The tessellation uses two unique unit cells shown in red and blue, with hinge lines rotated by $\frac{\pi}{2}$. (a) Side view of the tessellation. (b) Isometric view with the unfolded configuration. (c) Physical model.

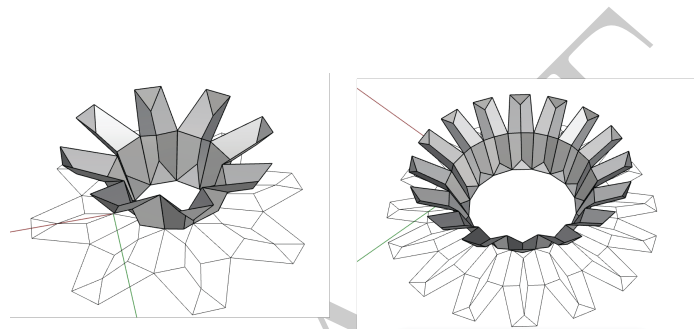


Figure 23: (a) Design for an 8 cell octopus ring. (b) Design for a 16 cell octopus ring. (c) 8 cell physical prototype. (d) 16 cell physical prototype.

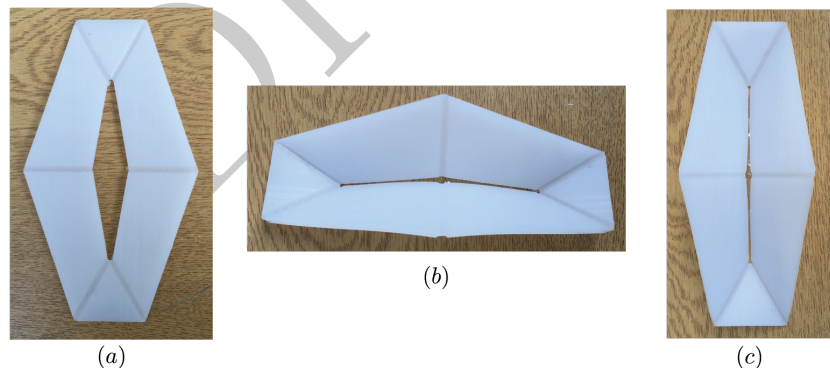


Figure 24: (a) Top view of the cell in the open configuration. (b) Side view of the cell in the closed configuration. (c) Top view of the cell in the closed configuration.

labeled geometric parameters. We dub this cell the “hexapus” unit. The kinematics of this cell are identical to the octopus cell; only the geometry is slightly changed, and all of the previous analysis still applies. As shown in Fig. 27, the hexagonal

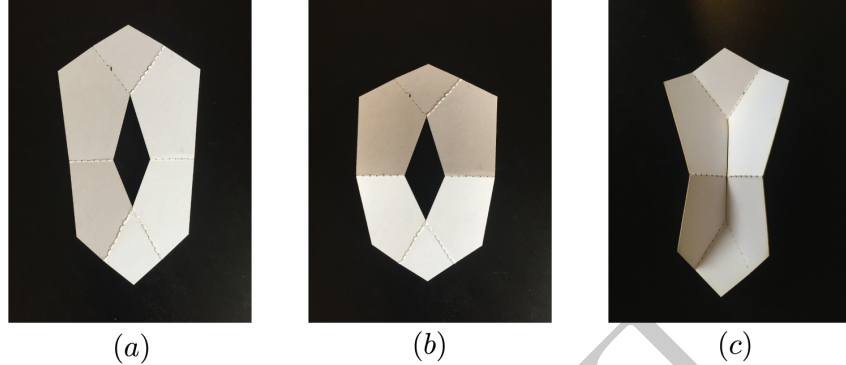


Figure 25: Paper prototype of a singly-symmetric octopus cell. (a) The open configurations. (b) The mode due to geometric hinge alignment, without compliance. (c) The closed, antisymmetric mode requiring facet compliance.

tessellation is a one degree of freedom structure capable of transforming between flat and singly-curved structures. The stiffness of the cylindrical shell shown here is based from the non-developable vertices created during the hole gluing process. The radius and length of the cylinder can be altered by the size of the tessellation and the cells’ geometric parameters. The internal shape of a tube with equal-sided hexagonal cells, where the internal cross section is a regular polygon of n sides corresponding to a tessellation n cells wide. The design parameter for a tessellation that closes exactly into a cylindrical structure is

$$\cos\left(\frac{\pi(n-2)}{n}\right) = -\frac{\cos 2\beta - \cos 2\alpha + \sin 2\alpha \sin 2\beta}{\cos(2\alpha + 2\beta) - 1} \quad (39)$$

invoking Eqn (30) and the interior angle formula for regular polygons. We can use the hexapus cell to create ring structures in the same manner as the octopus cell. This manner of tessellation can be used to create conical structures as shown in Fig. 28. Note that this singly symmetric unit cell will include a small degree of compliance in order to transform its shape. Thus, we can developed a tessellating kirigami unit cell that, through geometry prescription, can take a variety of forms while obeying a single kinematic relationship. We can imagine manufacturing many of these cells for use in deployable sheets where curvature is required. Utilizing the parameterizations

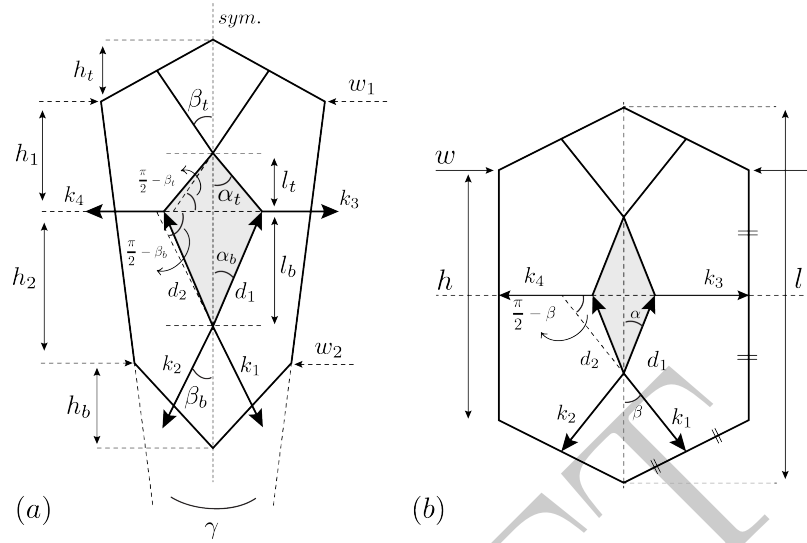


Figure 26: (a) A hexagonal octopus cell with unequal side lengths and only one symmetry plane. (b) A hexagonal unit cell with two symmetry planes.

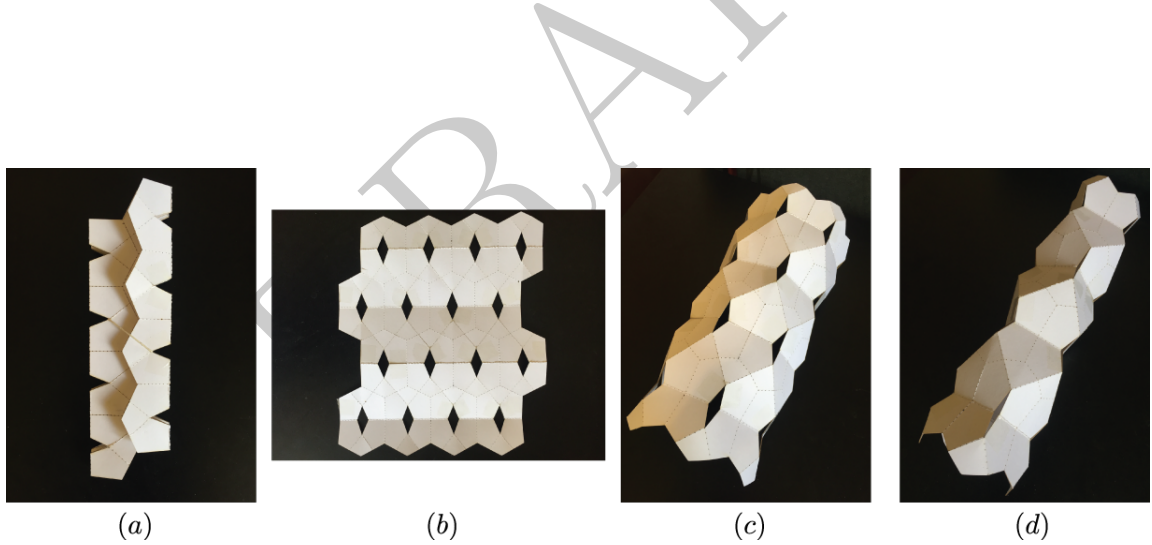


Figure 27: Design for a 2D tessellation of equal-sided hexagonal cells. (a) The flat-folded state. (b) Unfurled to the planar state. (c) The partial closed folded state. (d) The final, non-developable closed cylinder state.

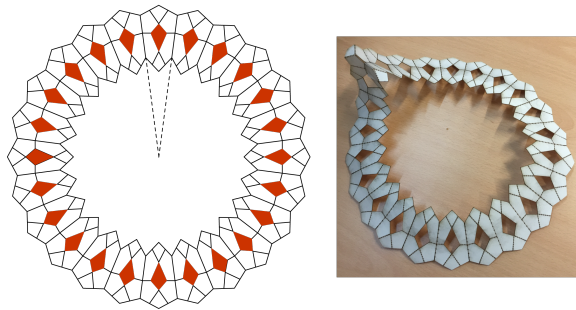


Figure 28: A 1D tessellation of singly-symmetric hexagonal cells. This cell can be used to create conical forms.

here, designs can be exactly calculated to achieve arbitrary, singly curved shapes. We can use both rigid folding techniques and create designs with a known amount of compliance depending on the symmetry of the desired structure.